



Synthesis of Efficient TMS@MOF-5 Catalysts for Oxygen Evolution Reaction

Muhammad Fiaz^{1,2} · Muhammad Kashif¹ · Misal Fatima¹ · Syeda Rabia Batool³ · Muhammad Adnan Asghar⁴ · Muhammad Shakeel⁵ · Muhammad Athar¹

Received: 5 November 2019 / Accepted: 20 February 2020 / Published online: 4 March 2020
© Springer Science+Business Media, LLC, part of Springer Nature 2020

Abstract

For environment friendly water splitting, development of highly efficient and stable oxygen evolution reaction (OER) catalyst composed of earth abundant elements is very challenging. Herein, highly efficient OER catalysts TMS@MOF-5 have been prepared by in-situ incorporation of pre-synthesized various transition metal sulfide (TMS = MnS, FeS, CoS, NiS, CuS and ZnS) nanoparticles into MOF-5. Structure, morphology and composition of prepared samples have been analyzed by powder X-ray diffraction, Fourier Transform Infrared Spectroscopy, Raman Spectroscopy, Scanning Electron Microscopy, Energy Dispersive X-ray Spectroscopy, Elemental Mapping and Ultraviolet–Visible Spectroscopy. OER activity of all these samples was determined by coating them on Ni-foam to form TMS@MOF-5/NF as working electrode through cyclic voltammetry. Among all the samples, NiS@MOF-5/NF exhibited excellent stability and OER catalytic activity as it required just 174 mV overpotential to achieve the 10 mA cm⁻² current density, which is better than many other 3d transition metal based and Ni-based OER catalysts. Present study provides new way to design more efficient Ni-based catalysts for electrochemical water splitting applications.

Electronic supplementary material The online version of this article (<https://doi.org/10.1007/s10562-020-03155-6>) contains supplementary material, which is available to authorized users.

✉ Muhammad Athar
athar.qr@bzu.edu.pk

¹ Institute of Chemical Sciences, Bahauddin Zakariya University, Multan 60800, Pakistan

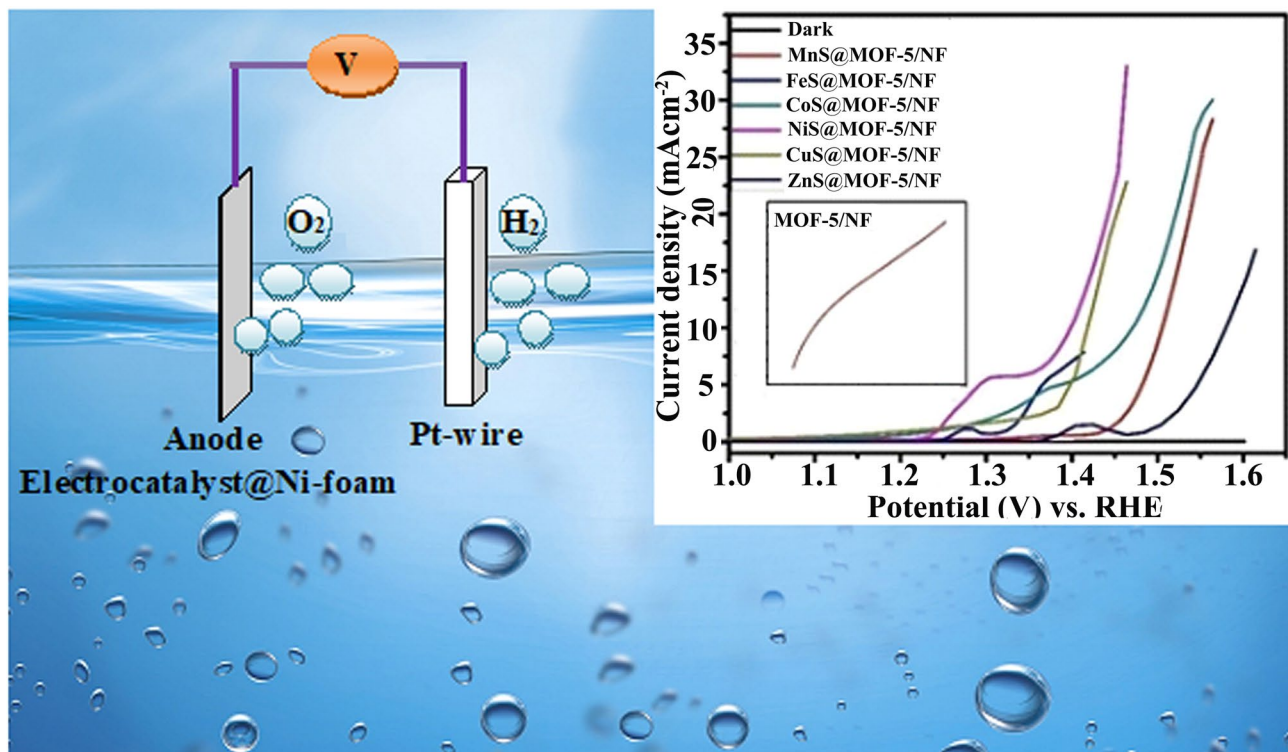
² School of Chemistry, University of Glasgow, Glasgow, UK

³ Institute for Chemical and Bioengineering, ETH Zurich, Zurich 8093, Switzerland

⁴ Department of Chemistry, Division of Science and Technology, University of Education Lahore, Lahore, Pakistan

⁵ Institute of Advanced Materials, Bahauddin Zakariya University, Multan 60800, Pakistan

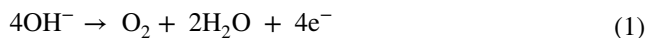
Graphic Abstract



Keywords Metal organic frameworks · Oxygen evolution reaction · Overpotential · Transition metal sulfide nanoparticles · Water oxidation

1 Introduction

Hydrogen is considered as most suitable alternative of petroleum to fulfill the energy demands of the World. The best known approach for hydrogen production is from water splitting due to its environmental benefits. Water splitting is divided into two-half reactions; oxygen evolution reaction (OER) at anode and hydrogen evolution reaction (HER) at cathode [1]. Both these reactions are kinetically sluggish and require a huge overpotential to generate hydrogen and oxygen. OER is more sluggish as compared to HER because it involves four-electron transfer reaction for O–H bond breaking and O–O bond formation [2].



At present, noble-metal based materials such as Pt for HER and Ru, Ir-based materials for OER are considered to be highly efficient catalysts due to negligible overpotential and high reaction kinetics [3]. But these catalysts cannot be applied at large scale due to high cost and low abundance. So, development of highly abundant, low cost and efficient HER and OER catalyst has attracted intensive research

attention. In recent years, scientists and researchers are more focused towards the development of efficient catalysts for OER as compared to HER [4].

Up to date, tremendous efforts have been made to develop efficient 3d-transition metal based OER catalysts such as selenides [5], oxides [6], sulfides [7], phosphides [8] and carbides [9] due to their low cost, natural earth abundance and environmental benefits. Among all 3d transition metals, phosphides, selenides and sulfides of Fe, Co and Ni have shown higher OER activity [10] such as FeCoNiO_x coated on Ni-foam (η_{10} = 203 mV) [11], CaCo₂O₄ nanoplate (η_{10} = 371 mV) [12], NiPS₃ nanosheets (η_{10} = 350 mV) [13], mesoporous CoFe₂O₄ (η_{10} = 342 mV) [14] and so on. Recently, Ni-based OER catalysts such as oxides, sulfides, selenides, phosphides, nitrides, oxyhydroxides, borides and borates have shown superior OER activity due to oxidation reaction of Ni²⁺ → Ni³⁺. It generates the NiOOH centers at surface of working electrodes, which act as active sites for oxygen generation and thus, lowers the overpotential for OER in alkaline solution [15, 16].

Among other 3d transition metal compounds, transition metal sulfides have diverse applications and have been

widely used in energy related applications such as in secondary batteries, supercapacitors, metal-air batteries, dye sensitized solar cells and water splitting for example MnCo_2S_4 has been reported as efficient OER catalyst [17]. Activity of alone 3d transition metal based catalysts is not at satisfactory level. Different strategies have been developed to improve their OER activity and one of them is the incorporation of transition metal based nanoparticles into MOFs. Metal organic frameworks (MOFs) due to their tunable composition, structure and morphologies have been widely used in gas adsorption, separation, luminescence, drug delivery, energy conversion and storage [18]. Up till now, a large number of MOFs based materials such as TMS@MOF-5 ($\text{TMS} = \text{MnSe}, \text{FeSe}, \text{CoSe}, \text{NiSe}, \text{CuSe}, \text{ZnSe}$) and $\text{M}_x\text{O}_y\text{@MIL-125(Ti)}$ ($\text{M}_x\text{O}_y = \text{Mn}_2\text{O}_3, \text{Fe}_2\text{O}_3, \text{Co}_3\text{O}_4, \text{NiO}, \text{CuO}$) have been reported as efficient catalysts towards both HER and OER [19]. Amongst different TMS@MOF-5 composites, MnSe@MOF-5/NF required just 170 mV overpotential to deliver benchmark of 10 mA cm^{-2} current density towards OER [20, 21]. Another highly efficient MOF-based catalyst reported is CuO@UiO-66/NF , which required only 220 mV overpotential to deliver -10 mA cm^{-2} current density towards HER [22].

Herein, we report a facile route for low cost and room temperature synthesis of TMS@MOF-5 ($\text{TMS} = \text{MnS}, \text{FeS}, \text{CoS}, \text{NiS}, \text{CuS}$ and ZnS) composites by in-situ incorporation of pre-synthesized transition metal sulfide (TMS) nanoparticles into MOF-5. The synthesized materials require lower overpotential and show superior OER activity in alkaline medium.

2 Experimental

2.1 Chemicals

All the chemicals used for the synthesis of TMS nanoparticles, bare MOF-5 and TMS@MOF-5 composites were purchased from Merck and these are Zinc acetate dihydrate, ($\text{Zn}(\text{CH}_3\text{COO})_2 \cdot 2\text{H}_2\text{O}$; 99.99%), 1,4-Benzenedicarboxylic acid (H_2BDC ; 98.0%), N,N-Dimethylformamide (DMF; 99.8%), Manganese(II) chloride (MnCl_2 ; 99.0%), Sodium sulfide nonahydrate ($\text{Na}_2\text{S} \cdot 9\text{H}_2\text{O}$; 99.99%), Ethylenediaminetetraacetic acid (EDTA; 99.99%), Iron(III) nitrate nonahydrate ($\text{Fe}(\text{NO}_3)_3 \cdot 9\text{H}_2\text{O}$; 99.99%), Sodium tartrate dihydrate ($\text{C}_4\text{H}_4\text{Na}_2\text{O}_6 \cdot 2\text{H}_2\text{O}$; 98.0%), Sodium thiosulfate pentahydrate ($\text{Na}_2\text{O}_3\text{S}_2 \cdot 5\text{H}_2\text{O}$; 99.5%), Hydrochloric acid (HCl; 37.0%), Cobalt(II) chloride hexahydrate ($\text{CoCl}_2 \cdot 6\text{H}_2\text{O}$; 98.0%), Thiourea (NH_2CSNH_2 ; 99.0%), Nickel (II) sulfate hexahydrate ($\text{NiSO}_4 \cdot 6\text{H}_2\text{O}$; 98.0%), Thioacetamide (CH_3CSNH_2 ; 99.0%), L-Cysteine ($\text{HSCH}_2\text{CH}(\text{NH}_2)\text{CO}_2\text{H}$; 98.5%), Copper(II) nitrate trihydrate ($\text{Cu}(\text{NO}_3)_2 \cdot 3\text{H}_2\text{O}$;

98.0%), Zinc nitrate hexahydrate ($\text{Zn}(\text{NO}_3)_2 \cdot 6\text{H}_2\text{O}$; 99.0%). All these reagents were used as such without any further purification.

2.2 Preparation of Transition Metal Sulfide (TMS) Nanoparticles

Six transition metal sulfide (TMS) nanoparticles ($\text{TMS} = \text{MnS}, \text{FeS}, \text{CoS}, \text{NiS}, \text{CuS}$ and ZnS) were prepared by using the methods reported previously in literature [22–28]. MnS nanoparticles were synthesized via precipitation method by using equimolar amount of manganese chloride and sodium sulfide nonahydrate in the presence of EDTA as capping agent. Similarly, FeS nanoparticles were also synthesized by mixing equimolar amount of iron(III) nitrate nonahydrate and sodium thiosulfate in 25 mL solution of 0.25 M sodium tartrate dihydrate, it acts as a complexing agent, via wet chemical reduction method. While, four TMS ($\text{CoS}, \text{NiS}, \text{CuS}$ and ZnS) nanoparticles were synthesized via hydrothermal method. In a typical reaction for the synthesis of these nanoparticles, a specific amount of metal ion and S^{2-} ion sources were dissolved separately in 25 mL deionized water via continuous stirring for 30 min. After that, the precursor solutions were mixed together and stirred for another 30 min. Finally, the entire mixture was transferred into 100 mL Teflon-lined stainless steel autoclave and kept in an oven at specific temperature for particular period of time, as mentioned in Table 1 for each sulfide product.

2.3 In-Situ Incorporation of TMS Nanoparticles into MOF-5

TMS@MOF-5 samples were prepared by in-situ incorporation of pre-synthesized TMS nanoparticles into MOF-5 at room temperature. Typically, to synthesize TMS@MOF-5 composites, 0.8 g of terephthalic acid (H_2BDC) was dissolved in 20 mL of N, N-dimethylformamide (DMF), followed by dropwise addition of 10 mL DMF suspension of 0.01 g TMS nanoparticles and stirred it for 30 min. After that 20 mL DMF solution of 2.7 g $\text{Zn}(\text{CH}_3\text{COO})_2 \cdot 2\text{H}_2\text{O}$ was added dropwise and stirred the whole mixture for 24 h at room temperature. The as-prepared precipitates of TMS@MOF-5 composites were separated by centrifugation, washed three times with DMF, dried overnight at 50°C in an oven under vacuum and ground the dried precipitates. Similarly, bare MOF-5 was also prepared without adding TMS nanoparticles. Dried precipitates of bare MOF-5 and TMS@MOF-5 were activated at 120°C for 6 h. Finally, the activated products were stored for further characterization and electrochemical studies.

Table 1 Brief summary of experimental conditions for hydrothermal synthesis of CoS, NiS, CuS and ZnS nanoparticles

Material	Metal ion source	Sulfide ion source	Temperature (°C)	Time (h)
CoS	CoCl ₂ ·6H ₂ O	Thiourea	180	24
NiS	NiSO ₄ ·6H ₂ O	Thioacetamide and L-Cysteine	120	4
CuS	Cu(NO ₃) ₂ ·3H ₂ O	Sodium thiosulfate pentahydrate	150	24
ZnS	Zn(NO ₃) ₂ ·6H ₂ O	Thiourea	170	3

2.4 Preparation of Working Electrodes

The working electrodes of all synthesized samples were prepared on a piece (1 cm × 1 cm) of Ni-foam. The piece of Ni-foam was cleaned by washing with acetone and deionized water, respectively. To prepare the working electrodes of prepared catalysts, 10 mg of TMS@MOF-5 samples were dispersed in 1 mL water and sonicated for 30 min to obtain uniformly dispersed slurry. The slurry was coated on pre-cleaned and dried piece of Ni-foam (1 cm × 1 cm) and kept it overnight at 50 °C.

2.5 Electrochemical Measurements Towards Oxygen Evolution Reaction (OER)

All the electrochemical measurements towards OER were performed via computer controlled AUTO LAB potentiostat (PGSTAT-204) by using conventional three-electrode setup in 1 M KOH aqueous solution as electrolyte. An Ag/AgCl electrode in 3 M KCl_{aq} as reference electrode, Pt-wire as counter electrode and prepared catalyst@Ni-foam as working electrode were used. To evaluate the catalytic activity toward OER, cyclic voltammetry (CV) and linear sweep voltammetry (LSV) measurements were performed at 30 mV s⁻¹ and 1 mV s⁻¹, respectively. All the obtained potential data vs. Ag/AgCl was converted into reversible hydrogen electrode (RHE) potential by using equation [29].

$$E_{\text{RHE}} = E_{\text{Ag/AgCl}} + 0.197 + 0.059 \text{ pH} \quad (2)$$

where, E_{RHE} = potential vs. RHE, $E_{\text{Ag/AgCl}}$ = potential measured vs. Ag/AgCl electrode and 0.197 V = standard Ag/AgCl electrode potential.

During OER activity, overpotential required to deliver the specific current density was calculated via following equation.

$$\text{For OER, } \eta = E_{\text{RHE}} - 1.23 \quad (3)$$

where, η = overpotential required to deliver a specific current density.

2.6 Tafel Slope Calculation

To understand the kinetics of OER, Tafel slope was calculated from Tafel plot. Tafel plot was derived from LSV measurements by using following equation.

$$\eta = a + b \log j \quad (4)$$

where, η = overpotential, a = charge transfer coefficient, b = Tafel slope and j = current density.

2.7 Electrochemical Stability of Working Electrodes

Electrochemical stability of working electrodes is an important parameter for their commercial applications. Therefore, electrochemical stability was evaluated by performing 1000 continuous CV sweeps. Further, stability of working electrodes was tested via Chronoamperometric measurements at constant applied voltage of 1.5 V for 600 s.

2.8 Characterizations of Synthesized Materials

Crystal structure of synthesized samples was evaluated by P-XRD patterns by using Shimadzu X-ray diffractometer with Cu-K α radiation ($\lambda = 0.15406$ nm) at 40 kV and 40 mA in 2 θ range between 5°–50°. FTIR spectra were obtained in wavelength range between 4000–400 cm⁻¹ by using Nicolet Nexus 870 spectrometer. Raman spectra were recorded in range 100–2000 cm⁻¹ on Jobin-Yvon LabRAM HR800 Raman Spectrometer ($\lambda = 532$ nm). Morphology and composition of synthesized samples were studied by Scanning electron microscopy (SEM) images, SEM based Energy Dispersive X-ray (EDX) images and Elemental Maps by using Philips XL30 Environmental SEM attached with an Oxford Instrument Inca 500 Energy Dispersive X-ray Spectrometer (EDX). Optical properties were measured by UV-Vis spectra, obtained by using Shimadzu UV-2600 spectrophotometer in range of 200–900 nm.

3 Results and Discussions

Formation of bare MOF-5 and TMS@MOF-5 composites were evaluated and confirmed by P-XRD patterns (Fig. 1). It is observed from P-XRD pattern of bare MOF-5 that the diffraction peaks of as-synthesized MOF-5 are matched well with previously reported pattern of MOF-5, which indicates the successful formation of Zn-based MOF (MOF-5) [30, 31]. It can also be observed from P-XRD pattern of MOF-5 that a diffraction peak is observed at $2\theta = 8.9^\circ$ due to moisture. However, in the P-XRD patterns of TMS@MOF-5 this peak is not observed, except for CoS@MOF-5. All the diffraction patterns have a characteristic diffraction peak of MOF-5 at $2\theta = 9.7^\circ$ but in the P-XRD patterns of TMS@MOF-5 composites another diffraction peak is also observed at $2\theta = 10.4^\circ$. It indicates that incorporation of TMS nanoparticles affects a little the crystal structure of bare MOF-5 during in-situ incorporation. In TMS@MOF-5 composites some additional diffraction peaks index to TMS (TMS = MnS, FeS, CoS, NiS, CuS and ZnS) nanoparticles are also observed. It is also revealed from the PXRD patterns of TMS@MOF-5 composites that the characteristic diffraction peaks of TMS nanoparticles are very less intense and overlaid by MOF-5, which indicates that host MOF remains intact and kept its dominance sufficiently during synthesis of TMS@MOF-5 composites. Furthermore, in all these diffraction patterns no extra peaks for impurity are observed, which shows the single phase formation of these materials.

FTIR spectroscopy was further used to verify the synthesis of bare MOF-5 and TMS@MOF-5, (Fig. 2). FTIR spectra

of MOF-5 show two prominent transmittance peaks at 1575 and 1370 cm^{-1} due to symmetric and asymmetric stretching vibrations of C–O groups on benzene ring. While the transmittance peaks observed in region between $850\text{--}600\text{ cm}^{-1}$ are due to in-plane and out of plane stretching vibrations of C–H group of benzene ring. Another small transmittance peak is found in FTIR spectra of MOF-5 at 642 cm^{-1} due to stretching vibration of $[\text{Zn}_4\text{O}]^{6+}$ cluster of MOF-5 [32]. In case of FTIR spectra of TMS@MOF-5 composites transmittance peaks are observed at 1575, 1370, 813, 744 cm^{-1} same as in bare MOF-5, which indicate that MOF-5 remains intact after incorporation of TMS nanoparticles. Very weak transmittance peaks due to stretching vibrations of Mn–S, Fe–S, Co–S, Ni–S, Cu–S and Zn–S are also found in FTIR spectra of TMS@MOF-5 samples at 620, 528, 617, 618, 630 and 619 cm^{-1} , respectively [33–37]. Presence of faint transmittance peaks for TMS indicate occurrence of weak van der Waals interaction between incorporated TMS nanoparticles and MOF-5. It can also be observed from FTIR spectra of bare MOF-5 that it contains a less intense and weak transmittance peak at 3605 cm^{-1} due to presence of DMF molecules [38]. While in FTIR spectra of TMS@MOF-5 composites, as a result of successful incorporation of TMS nanoparticles, no transmittance peak related to DMF at 3605 cm^{-1} is observed.

Further, Raman spectroscopy was used to explore the structure of MOF-5 and changes in crystal structure as a result of incorporation of TMS nanoparticles. Raman spectra of bare MOF-5 and TMS@MOF-5 composites are presented

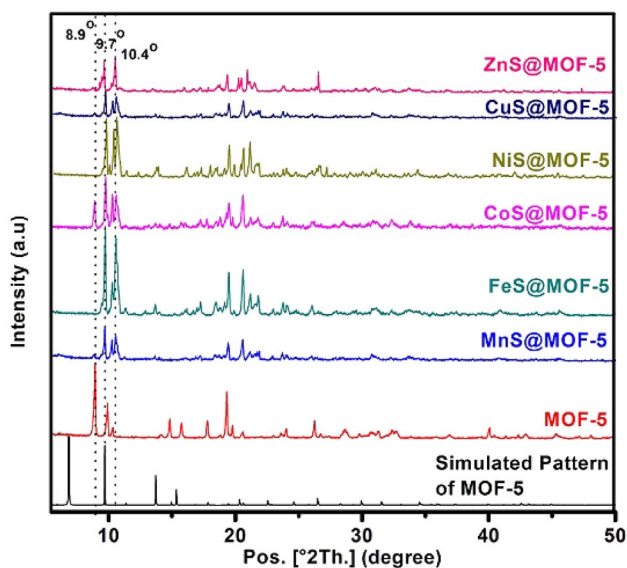


Fig. 1 P-XRD patterns of bare MOF-5 and TMS@MOF-5 composites

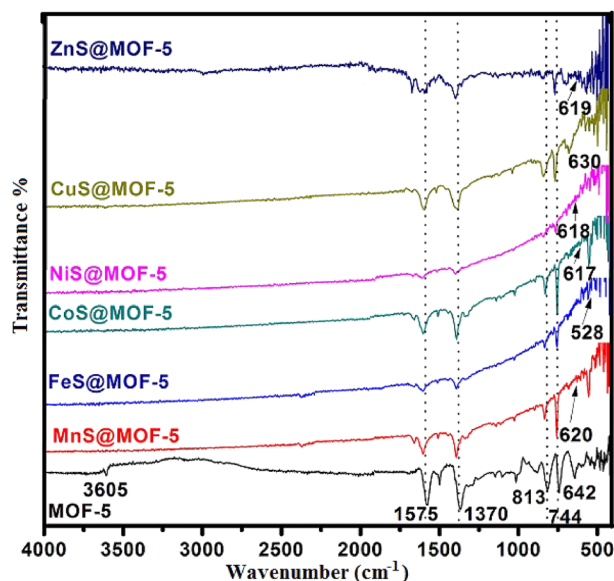


Fig. 2 FTIR spectra of bare MOF-5 compared with TMS@MOF-5

in Fig. 3. Laser excitation created five major Raman bands at 1615, 1433, 1140, 866 and 635 cm^{-1} in MOF-5, which primarily correspond to vibrational modes of COO – group and aromatic benzene ring of organic ligand [39]. In the same way, Raman spectra of TMS@MOF-5 also contain same Raman bands as in MOF-5 and no major changes are observed due to incorporation of TMS nanoparticles. It indicated that incorporation of TMS nanoparticles did not disturb the crystalline structure of MOF-5.

SEM images were used to analyze the morphology of synthesized samples of bare MOF-5 and TMS@MOF-5 composites, shown in Fig. 4a–g. SEM image of bare MOF-5 reveals that it has smooth surface with rectangular shaped crystalline structure (Fig. 4a). While the SEM images of TMS@MOF-5 show that as a result of incorporation of TMS nanoparticles, irregularities are observed both in shape and size and exhibit coarse surfaces except NiS@MOF-5 which have smooth surface and uniformly distributed cubic shaped crystalline structure Fig. 4b–g. To investigate the distribution of incorporated particles of TMS into MOF-5, SEM based Elemental mapping was used. Elemental maps of bare MOF-5 and TMS@MOF-5 are shown in Fig. 4a'–g'. Figure 4a' represents the elemental map of bare MOF-5 and distribution of basic elements Zn, C and O of MOF-5 are represented by red, blue and green color, respectively. It indicates that all the building elements of MOF-5 are uniformly distributed in rectangular shaped crystalline structure. Figure 4b'–g' represents the elemental maps of MnS@MOF-5, FeS@MOF-5, CoS@MOF-5, NiS@MOF-5, CuS@MOF-5 and ZnS@MOF-5, respectively. In the elemental maps of TMS@MOF-5, from MnS@MOF-5 to CuS@MOF-5, distribution of Zn from MOF-5, S and transition metal (Mn, Fe, Co, Ni and Cu respectively) from TMS nanoparticles are represented via blue, green and red color,

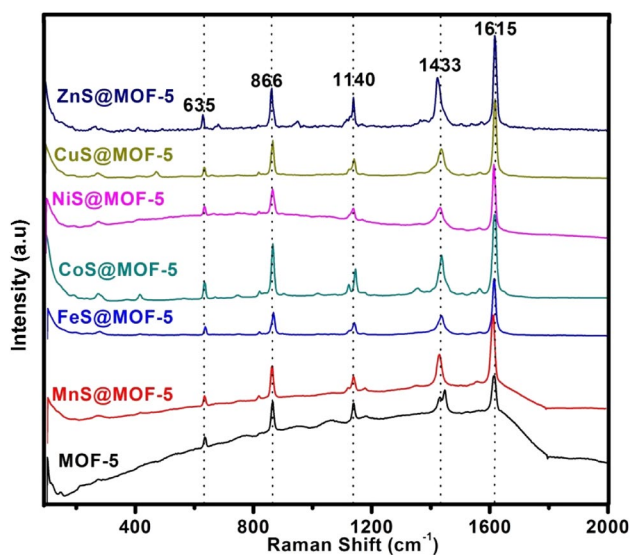


Fig. 3 Raman spectra of bare MOF-5 compared with TMS@MOF-5

respectively. While in the case of ZnS@MOF-5 distribution of basic elements Zn, C and S are represented by red, blue and green color, respectively. Further, Elemental maps of TMS@MOF-5 reveal that the incorporated particles are also uniformly distributed in MOF-5. Individual elemental maps of all the distributed elements in bare MOF-5 and TMS@MOF-5 composites are shown in Fig. S1.

Presence of different elements in synthesized samples was determined by energy dispersive X-ray (EDX) analysis. SEM based recorded EDX spectra of all synthesized samples are presented in Fig. S2a–g. According to EDX results, all the synthesized samples contain basic diffraction peaks of Zn, C and O from metal organic framework (MOF-5) as well as additional peaks of Mn, Fe, Co, Ni, Cu and Zn for MnS@MOF-5, FeS@MOF-5, CoS@MOF-5, NiS@MOF-5, CuS@MOF-5 and ZnS@MOF-5 respectively. So, the comparison of EDX spectra of bare MOF-5 and TMS@MOF-5 indicate that targeted TMS@MOF-5 composites were successfully synthesized without any impurity and in single phase.

UV–Vis spectrophotometry was used to analyze the optical absorption of synthesized samples, (Fig. 5a). UV–Vis spectrum of MOF-5 show strong absorption in UV region with λ_{max} at 265 nm. It is shifted towards shorter wavelength in range of 213–233 nm in TMS@MOF-5 samples due to incorporation of TMS nanoparticles and absorption edge is also shifted towards visible region upto 520 nm. Further, the Tauc plot is derived from UV–Vis spectra by using the standard Tauc's relation;

$$(\alpha h\nu)^n = A(h\nu - E_g) \quad (5)$$

where, α = absorption coefficient, $h\nu$ = photon energy, A = optical transition dependent constant, E_g = optical band gap. Direct optical band gaps of bare MOF-5 and TMS@MOF-5 are obtained by extrapolating the tangent of the Tauc plot and it is found to be 4.06 eV for MOF-5 and 3.59, 2.81, 2.87, 2.56, 3.83, 3.92 eV, respectively for MnS@MOF-5, FeS@MOF-5, CoS@MOF-5, NiS@MOF-5, CuS@MOF-5 and ZnS@MOF-5. So, this analysis indicates that incorporation of TMS nanoparticles into MOF-5, shifted the band gap more towards visible region and enhanced the absorption of visible region of electromagnetic radiations in TMS@MOF-5 as compared to bare MOF-5. Figure 5b represents the Tauc plot of both bare MOF-5 and TMS@MOF-5 samples.

4 Electrochemical Analysis for Oxygen Evolution Reaction (OER) Studies

To understand the catalytic OER characteristics of bare MOF-5/NF and TMS@MOF-5/NF working electrodes, cyclic voltammetry (CV) and linear sweep voltammetry

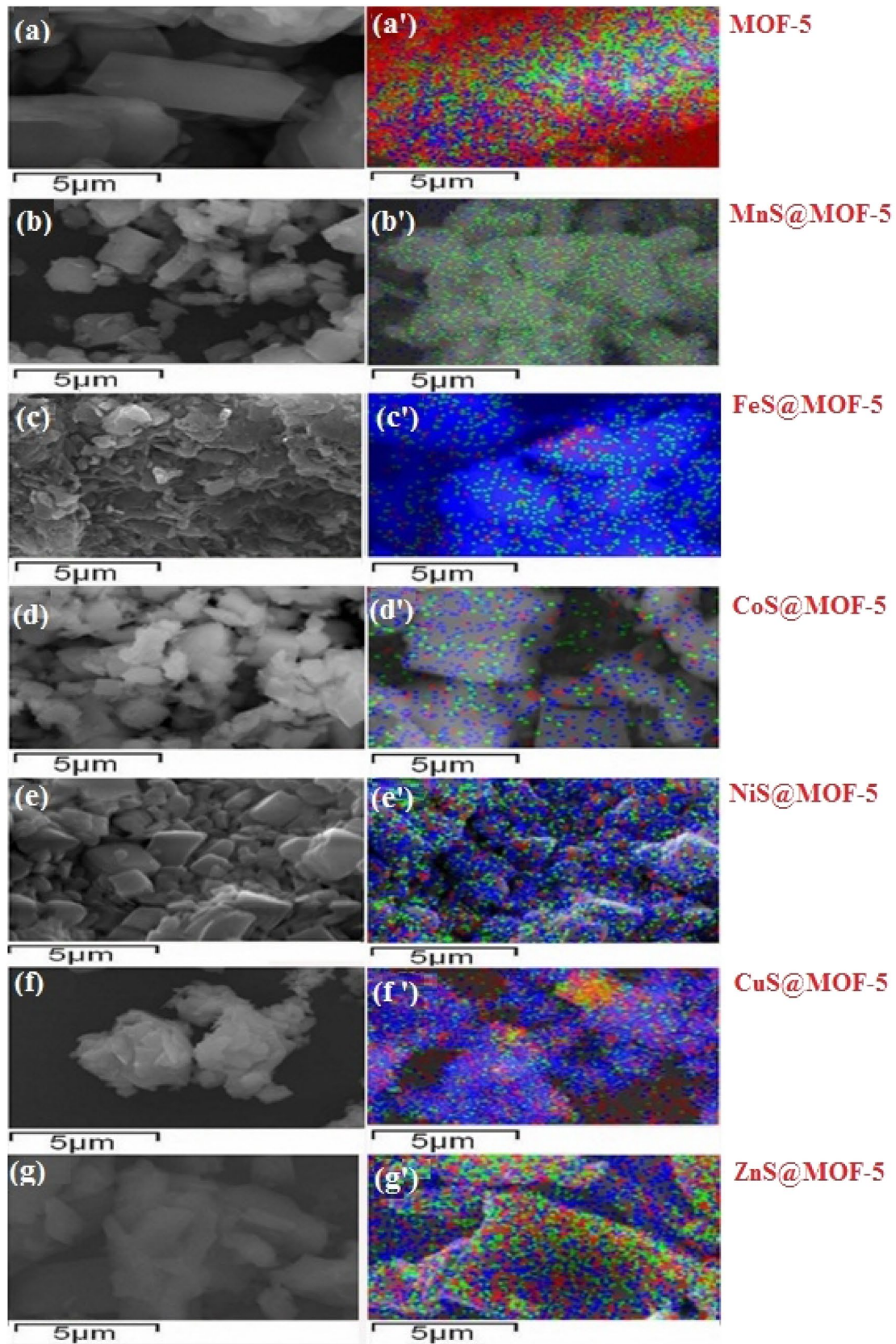


Fig. 4 a–g SEM images and a'–g' SEM based Elemental maps of bare MOF-5 and TMS@MOF-5 composites

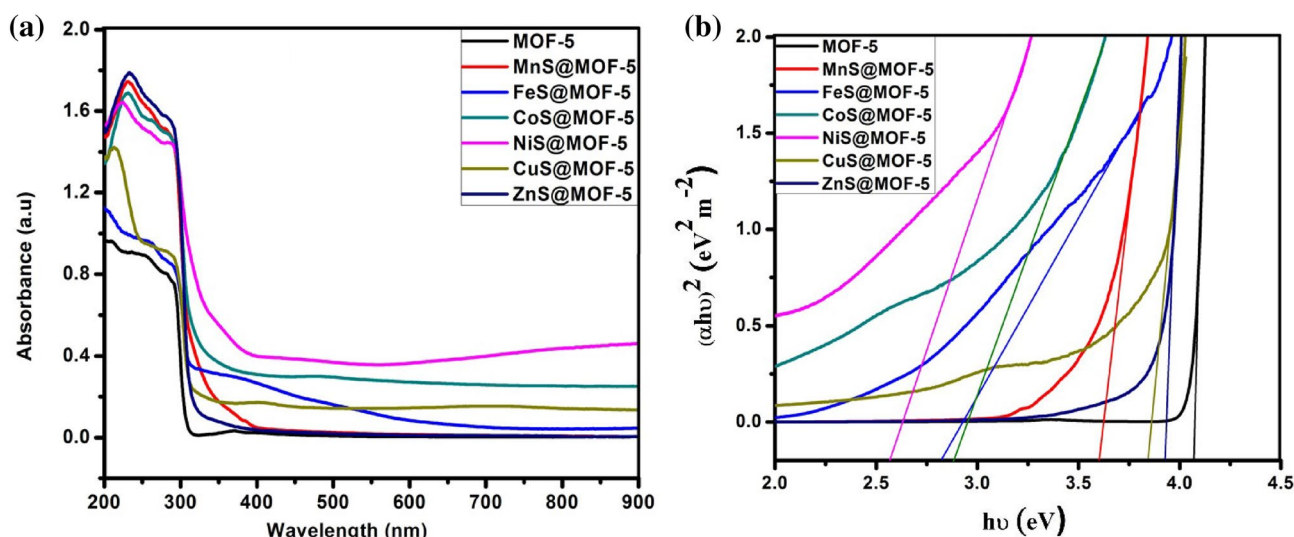


Fig. 5 **a** UV-Vis spectra and **b** Tauc plot of bare MOF-5 compared with TMS@MOF-5

(LSV) were performed both under dark and light. Figure 6a, compares the CV curves of TMS@MOF-5/NF and inset is the CV curve of bare MOF-5/NF. From the CV curve of MOF-5/NF it appears that MOF-5/NF did not generate any OER onset. Similarly, all the TMS@MOF-5/NF generated almost zero current density for OER under dark while in the presence of visible light pre-OER oxidation peaks are observed at potential range of 1.27–1.48 V (vs. RHE) in all samples due to release of Ni^{2+} from Ni-foam and oxidation of $\text{Ni}^{2+} \rightarrow \text{Ni}^{3+}$ at surface of working electrode and this pre-OER peaks play an important role to promote and enhanced OER activity. After the pre-OER peaks, sharp OER onset potentials are observed in all working electrodes at higher potentials. Among all the working electrodes, NiS@MOF-5/NF show the lowest OER onset potential with maximum OER current density of 23.69 mA cm^{-2} as compared to MnS@MOF-5/NF (14.45 mA cm^{-2}), FeS@MOF-5/NF (11.45 mA cm^{-2}), CoS@MOF-5/NF (19.15 mA cm^{-2}), CuS@MOF-5/NF (7.64 mA cm^{-2}) and ZnS@MOF-5 (18.62 mA cm^{-2}). Further, OER activity is compared by LSV measurements at 1 mV s^{-1} scan rate. Figure 6b, compares the LSV curves of TMS@MOF-5/NF working electrodes and inset is the LSV curve of MOF-5/NF. Like CV, in dark pure MOF-5/NF and all TMS@MOF-5/NF working electrodes generated almost zero current density and no OER onset potential is observed. Pre-OER oxidation peaks are observed in most of TMS@MOF-5/NF working electrodes due to oxidation of $\text{Ni}^{2+} \rightarrow \text{Ni}^{3+}$ in the presence of visible light, same as in CV analysis. To compare the OER performance, overpotential required to obtain the 5 mA cm^{-2} current density is considered. An overpotential of just 64 mV is measured to reach the current density of 5 mA cm^{-2} by NiS@MOF-5/NF than those of MnS@

MOF-5/NF ($\eta_5 = 253 \text{ mV}$), FeS@MOF-5/NF ($\eta_5 = 144 \text{ mV}$), CoS@MOF-5/NF ($\eta_5 = 154 \text{ mV}$), CuS@MOF-5/NF ($\eta_5 = 174 \text{ mV}$) and ZnS@MOF-5/NF ($\eta_5 = 314 \text{ mV}$). Except FeS@MOF-5/NF, all other TMS@MOF-5/NF working electrodes reach to benchmark 10 mA cm^{-2} current density at higher overpotential. Figure 6c, represents the overpotential required to achieve 10 mA cm^{-2} current density and it can be observed that NiS@MOF-5/NF requires only 174 mV overpotential to obtain 10 mA cm^{-2} current density which reach at 30 mA cm^{-2} at only 230 mV overpotential as compared to MnS@MOF-5/NF ($\eta_{10} = 276 \text{ mV}$), CoS@MOF-5/NF ($\eta_{10} = 253 \text{ mV}$), CuS@MOF-5/NF ($\eta_{10} = 194 \text{ mV}$) and ZnS@MOF-5/NF ($\eta_{10} = 354 \text{ mV}$). From LSV curves, it is observed that among all the TMS@MOF-5/NF working electrodes, NiS@MOF-5/NF show lowest OER onset potential, lowest η_5 and η_{10} and highest current density than others. This overpotential value of NiS@MOF-5/NF is amazingly superior then many of previously reported Ni-based OER catalysts and even better than state-of-the-art OER catalyst, which required 290 mV overpotential to deliver benchmark of 10 mA cm^{-2} current density, as shown in Table 2.

This comparative chart indicates that NiS@MOF-5/NF initiates the water oxidation at lowest overpotential relative to other Ni-based OER catalysts. Further, overpotential required to deliver benchmark of 10 mA cm^{-2} is comparable and even better than previously reported Ni based and MOFs based OER catalyst. The higher catalytic activity of NiS@MOF-5/NF is expected due to hetrojunction formation between central metallic cluster of MOF-5 and incorporated NiS nanoparticles. This hetrojunction formation gradually changes the electronic band structure and alignment of valence and conduction band edges with

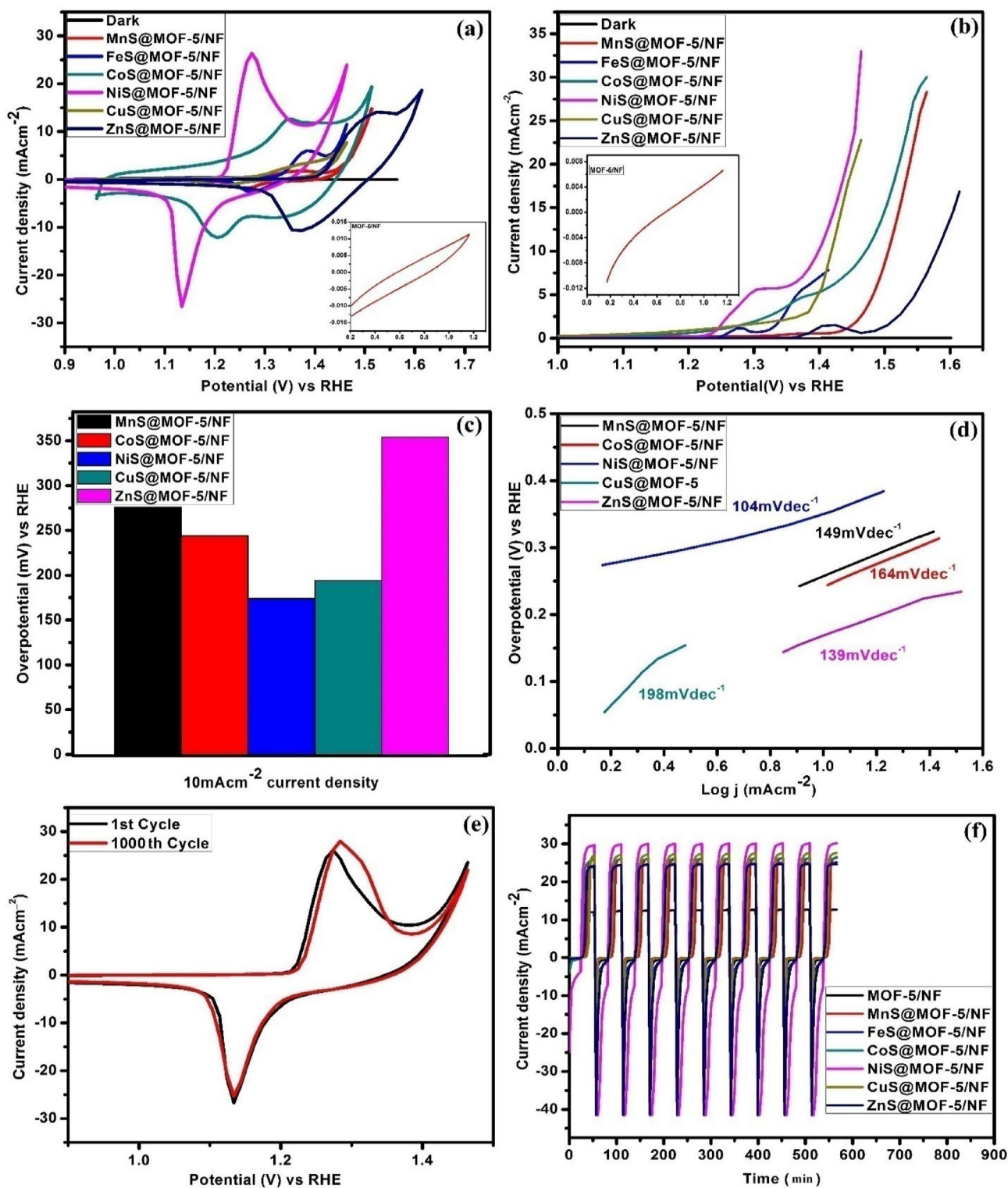


Fig. 6 **a** CV curves and **b** LSV curves of TMS@MOF-5/NF at 30 mV s⁻¹ and 1 mV s⁻¹, respectively and Inset is the CV and LSV of MOF-5/NF; **c** Overpotential for 10 mA cm⁻² current density; **d** Tafel

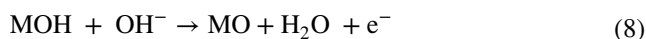
Plot of TMS@MOF-5/NF except FeS@MOF-5/NF; **e** 1st and 100th CV cycle for NiS@MOF-5/NF; **f** Chronoamperometric measurements of TMS@MOF-5/NF at 1.5 V for 600 s

Table 2 Comparison of OER performances for different OER catalysts in 1 M KOH electrolyte

Catalyst	Substrate	η for 10 mA cm ⁻² (mV)	References
FeCoNiO _x	Ni-foam	203	Materials Today Energy (2019) 12, 311–317
FeCoNiO _x	GC-carbon	240	Materials Today Energy (2019) 12, 311–317
NiFeOOH	GC	340	Journal of Physical Chemistry C (2015) 119, 19,022–19,029
Ni _{0.75} Fe _{0.25} OOH	GC	258	ACS Catalysis (2015) 5, 6680–6689
Nickel–cobalt nitride	Carbon cloth	247	Journal of Materials Chemistry (2018) 6, 4466–4476
Ni _{0.6} Fe _{0.3} Cr _{0.1} O _x	Carbon cloth	251	Electrochimica Acta (2018) 265, 10–18
NiPS ₃	–	350	ACS Catalysis (2017) 7, 229–237
NiS@MOF-5	Ni-foam	174	This work

oxidation–reduction potential. In this way, NiS@MOF-5/NF favorably initiates the water oxidation at lower onset potential and requires lower overpotential at 10 mA cm⁻² as compared to other OER catalyst. Furthermore, higher catalytic activity is also due to immobilization of NiS@MOF-5 on conductive Ni-foam substrate, which further supports optimum charge transfer during OER activity.

Corresponding Tafel plots (η vs. $\log j$) imparted more understanding about the reaction kinetics (Fig. 6d). NiS@MOF-5/NF has smallest Tafel slope of 104 mV dec⁻¹ than others MnS@MOF-5/NF (149 mV dec⁻¹), CoS@MOF-5/NF (164 mV dec⁻¹), CuS@MOF-5/NF (198 mV dec⁻¹) and ZnS@MOF-5/NF (139 mV dec⁻¹) and fastest OER performance as compared to others. Following is the widely accepted four step OER mechanism for oxygen evolution.



Furthermore, 1000 continuous CV sweeps are run at 30 mV s⁻¹ to evaluate the stability of NiS@MOF-5/NF and the CV curves did not show any significant loss in the current density or increase in overpotential after 1000 continuous CV cycles (Fig. 6e). Long-term stability of all working electrodes is studied by Chronoamperometric measurements in the presence of visible light by applying a constant voltage of 1.5 V for 600 min (Fig. 6f). All the working electrodes generated stable current density for specific period of time without any degradation. Same as in CV and LSV, NiS@MOF-5/NF generate maximum current density as compared to other TMS@MOF-5/NF samples. The maximum OER activity of NiS@MOF-5/NF can be explained by the fact that in most of Ni-based catalysts or 3d transition metal based OER catalysts coated on Ni-foam,

pre-OER oxidation peaks are observed in the potential range of 1.25–1.45 V due to Ni²⁺ to Ni³⁺ oxidation and formation of Ni–OOH or sometime M–OOH active sites at surface of working electrodes. These pre-OER peaks are closely related to OER activity and the current density or peak area of pre-OER peak indicate the amount of active sites (Ni–OOH/M–OOH) present at surface of working electrode, which corresponded to OER activity of catalyst [40]. In Ni-based catalysts, OER activity occurs in four steps; oxidation of Ni-atoms to Ni–OOH at surface of working electrodes in alkaline medium, further oxidation of Ni–OOH to NiO(OH)₂ and NiOO₂ at higher potential and at further higher potential NiOO₂ generate bubbles of O₂ at surface of working electrode leaving behind the NiOOH active species. Formation of NiOOH, NiO(OH)₂ and NiOO₂ is considered to be rate determining step in OER activity.

5 Conclusion

In this research, TMS@MOF-5 composites are successfully synthesized via in-situ incorporation of TMS into MOF-5 and it is believed that a hetero-junction is formed between incorporated TMS nanoparticles and [Zn₄O]⁶⁺ cluster of MOF-5 which plays an important role in decreasing the immediate recombination of electron–hole pair, shifts the optical band gap more towards visible region and enhances the absorption of visible light. TMS@MOF-5 composites are coated on Ni-foam to form TMS@MOF-5/NF working electrodes for OER performance. Systematic comparison of OER catalytic activity, morphology and composition reveals that NiS@MOF-5/NF is a highly efficient OER catalyst and it requires just 174 mV overpotential to deliver the 10 mA cm⁻² current density. So, these results provide the direction and guideline to form highly efficient materials by incorporated nanoparticles into metal organic frameworks for OER catalysis.

Acknowledgements The authors thank to Higher Education Commission (HEC) of Pakistan for providing financial support to carry out this project under International Research Support Initiative Program (IRSIP). We also acknowledge the use of lab facilities at School of Chemistry, University of Glasgow, UK, by Prof. Duncan H. Gregory.

Compliance with Ethical Standards

Conflict of interest The authors declare no conflict of interest.

References

- Harsharaj SJ, Animesh R, Gaurav MT, Wook CJ, Jeong SG (2019) Hierarchical free-standing networks of MnCo_2O_4 as efficient electrocatalyst for oxygen evolution reaction. *J Ind Eng Chem* 71:452–459
- Xiaohui D, Harun T (2014) Cobalt-oxide-based materials for water oxidation catalyst: Recent progress and challenges. *ACS Catal* 10:3701–3714
- Boon SY, Alexis TB (2011) Enhanced activity of gold-supported cobalt oxide for the electrochemical evolution of oxygen. *J Am Chem Soc* 14:5587–5593
- Jiao F, Frei H (2009) Nanostructured cobalt oxide clusters in mesoporous silica as efficient oxygen-evolution catalysts. *Angewandte Chemie, Int Ed* 48:1841–1844
- Hou W, Zheng B, Qi F, He J, Zhang W, Chen Y (2018) Graphene wrapped self-assembled $\text{Ni}_{0.85}\text{Se-SnO}_2$ microspheres as highly efficient and stable electrocatalyst for hydrogen evolution reaction. *Electrochimica Acta* 283:1146–1153
- Zhao B, Zheng Y, Ye F, Deng X, Xu XM, Liu ML, Shao Z (2015) Multifunctional iron oxide nanoflake/graphene composites derived from mechanochemical synthesis for enhanced lithium storage and electrocatalysis. *ACS Appl Mat Interfaces* 26:14446–14455
- Luo Y, Li X, Cai X, Zou X, Kang F, Cheng HM, Liu B (2018) Two-dimensional MoS_2 confined Co(OH)_2 electrocatalysts for hydrogen evolution in alkaline electrolytes. *ACS Nano* 12:4565–4573
- Yingjiong L, Wenqiang H, Dongxu Y, Yuanfu C (2019) CoP nanosheets in-situ grown on N-doped graphene as an efficient and stable bifunctional electrocatalyst for hydrogen and oxygen evolution reactions. *Electrochimica Acta* 307:543–552
- Hu Y, Guan D, Yu B, Hou W, Zheng B, Chen Y (2018) Scalable synthesis of $\text{Mo}_2\text{C/CNT}$ networks as highly efficient and stable electrocatalyst for hydrogen evolution reaction. *Electrochimica Acta* 263:192–200
- Ping L, Rai NA, Jing L, Guojing H, Xingqun Z, Yalin L, Bin X (2019) Self-reconstruction in 2D nickel thiophosphate nanosheets to boost oxygen evolution reaction. *Appl Surf Sci* 484:54–61
- Lu B, Xudong W, Jingqi G (2019) Amorphous Fe-Co-Ni oxide for oxygen evolution reaction. *Mater Today Energy* 12:311–317
- Xiao L, Jing Z, Dehua Z, Chengzhi G, Guoping X, Ning C, Qing L, Hongliang B, Qiang WJ (2019) Rational synthesis of CaCo_2O_4 nanoplate as an earth abundant electrocatalyst for oxygen evolution reaction. *J Energy Chem* 31:125–131
- Konkena B, Masa J, Botz AJR, Sinev I, Xia W, Kobmann J, Drautz R, Muhler M, Schuhmann W (2017) Metallic $\text{NiPS}_3@ \text{NiOOH}$ core-shell heterstructure as highly efficient and stable electrocatalyst for the oxygen evolution reaction. *ACS Catal* 7:229–237
- Yarong H, Weiwei Y, Yongsheng Y, Sue H (2019) Ordered mesoporous spinel CoFe_2O_4 as efficient electrocatalyst for the oxygen evolution reaction. *J Electroanal Chem* 840:409–414
- Yong L, Liangsheng H, Weiran Z, Xiang P, Mengjie L, Paul CK, Lawrence LSY (2018) Ni/Co-based nanosheet arrays for efficient oxygen evolution reaction. *Nano Energy* 52:360–368
- K. Sun, F.H.Saadi, M.F. Lichterman, W.G. Hale, H.P. Wang, X. Zhou, N.T. Plymale, S.T.Omelchenko, J.H. He, K.M. Papadantonaksi, B.S.Brunschwig, N.S. Lewis, Stable solar-driven oxidation of water by semiconducting photoanodes protected by transparent catalytic nickel oxide films. *Proc Nat Acad Sci USA* (2015) 112. 3612–3617.
- Dandan H, Yingying Z, Jian L, Yike H, Dongsheng L, Tao W (2017) Dual emissions from MnS clusters confined in the sodalite nanocage of a chalcogenide-based semiconductor zeolite. *Dalton Trans* 46:3929–3933
- Junxia G, Ming G, Jun N, Fengxiang Y, Guiping M (2019) ZIF-67/PAN-800 bifunctional electrocatalyst derived from electrospun fibers for efficient oxygen reduction and oxygen evolution reaction. *J Coll Interface Sci* 544:112–120
- Mahmood A, Guo W, Tabassum H, Zou R (2016) Metal-organic framework-based nanomaterials for electrocatalysis. *Adv Energy Mater* 6:1600423
- Fiaz M, Athar M (2019) Facile room temperature in situ incorporation of transition metal selenide (TMSe) nanoparticles into MOF-5 for oxygen evolution reaction. *JOM* 2019:1–7
- Fiaz M, Athar M (2019) Modification of MIL-125(Ti) by incorporation various transition metal oxide nanoparticles for enhanced photocurrent during hydrogen and oxygen evolution reaction. *Chem Sel* 4:8508–8518
- Fiaz M, Athar M, Rani S, Najam-ul-Haq M, Farid MA (2020) One pot solvothermal synthesis of $\text{Co}_3\text{O}_4@ \text{UiO-66}$ and $\text{CuO}@ \text{UiO-66}$ for improved current density towards hydrogen evolution reaction. *Mater Chemi Phys* 239:122320
- Shabna S (2017) Synthesis, confirmation and characterization of MnS nanocomposites. *Int J Sci Res* 6:910–912
- Tasmira MJ, Sunil CH, Deshpande MP (2018) Structural, morphological, optical, thermal and magnetic study of mackinwite FeS nanoparticles synthesized by wet chemical reduction technique. *Physica B: Condens Matter* 546:59–66
- Karthikeyan K, Ganesh VK, Sang KJ (2015) Hydrothermal synthesis, characterization and electrochemical properties of cobalt sulfide nanoparticles. *Mater Sci Semicond Process* 40:781–786
- Bandari N, Dinah P, Srinivasa RS, Archana S, Raja RB, Hee JK (2018) Hydrothermal synthesis and pseudocapacitive properties of morphology-tuned nickel sulfide (NiS) nanostructures. *New J Chem* 42:2733–2742
- Murugan S, Chella S, Rajendran R, Andrews GN (2014) Growth of CuS nanostructures by hydrothermal route and its optical properties. *J Nanotechnol* 2014:8
- Jayalakshmi M, Rao MM (2006) Synthesis of zinc sulphide nanoparticles by thiourea hydrolysis and their characterization for electrochemical capacitor applications. *J Power Sources* 157:624–629
- Fiaz M, Kashif M, Majeed S, Ashiq MN, Farid MA, Athar M (2019) Facile fabrication of highly efficient photoelectrocatalysts $\text{M}_x\text{O}_y@ \text{NH}_2\text{-MIL-125}$ for enhanced hydrogen evolution reaction. *Chem Sel* 4:6996–7002
- Yi L, Yue Q, Hongyi G, Radoelizo AS, Nannan Z, Ge W (2015) A general post-synthetic modification approach of amino-tagged metal-organic frameworks to access efficient catalysts for the Knoevenagel condensation reaction. *J Mater Chem A* 3:17320
- Ullah S, Bustam MA, Shariff AM, Eikhalfah AEI, Murshid G, Riaz N (2014) Synthesis and CO_2 adsorption study of modified MOF-5 with multi-wall carbon nanotubes and expandable graphite. *AIP Conf Proc* 34:1621
- Sabouni R, Kazemian H, Rohani S (2010) A novel combined manufacturing technique for rapid production of IRMOF-1 using ultrasound and microwave energies. *Chem Eng J* 165:966–973

33. Jing M, Yizhe Z, Zhongfeng L, Ligang W, Yang T (2016) Phase transfer preparation of ultrasmall MnS nanocrystals with high performance of MRI contrast agent. *RSC Adv* 6:6878–6887
34. H.Y. He Efficient interface-induced effect of novel reduced graphene oxide-CoS hetero nano structures in enhancing photocatalytic activities. *Appl Surf Sci* (2016) 421:260–267.
35. Mohanraj V, Jayaprakash R, Robert R, Balavijavalakshmi J, Gopi S (2016) Effect of particle size on optical and electrical properties in mixed CdS and NiS nanoparticles synthesis by ultrasonic wave irradiation method. *Mater Sci Semicond Process* 56:394–402
36. Subramanyam K, Sreelekha N, Reddy DA, Murali G, Varma KR, Vijayalkshmi RP (2017) Chemical synthesis, structural, optical, magnetic characteristics and enhanced visible light active photocatalysis of Ni doped CuS nanoparticles. *Solid State Sci* 65:68–78
37. Mozghan R, Ahmad H, Elaheh M (2018) *Penaeus vannamei* protease stabilizing process of ZnS nanoparticles. *Int J Biol Macromol* 112:509–515
38. Huang L, Wang H, Chen J, Wang Z, Sun J, Zhao D (2003) Synthesis, morphology and properties of porous metal-organic coordination polymers. *Micropor Mesopor Mater* 58:105–114
39. Hu HY, Zhang L (2010) Amorphization of metal organic framework MOF-5 at unusually low applied pressure. *Phys Rev B* 81:174103–174107
40. Yong L, Liangsheng H, Weiran Z, Xiang P, Mengjie L, Paul CK, Lawrence LSY (2018) Ni/Co-based nanosheets arrays for efficient oxygen evolution reaction. *Nano Energy* 52:360–368

Publisher's Note Springer Nature remains neutral with regard to jurisdictional claims in published maps and institutional affiliations.